JOURNAL OF SPACECRAFT AND ROCKETS
Vol. 35, No. 5, September–October 1998

Integrated Solution for Computational Static Aeroelasticity of Rockets

Mordechay Karpel*
Technion—Israel Institute of Technology, Haifa 32000, Israel
and
Sara Yaniv† and David S. Livshits‡
Israel Military Industries, Ramat Hasharon 47100, Israel

A solution scheme for computational static aeroelastic problems of maneuvering flight vehicles, with linear structure and nonlinear aerodynamics, is presented. A general steady computational fluid dynamics code that can handle both Navier-Stokes and Euler formulations is modified to include aeroelastic effects. A modal representation of the free structure is imported from a standard finite element code and integrated in the regular computation convergence scheme. The integrated process can solve direct problems with given aerodynamic states or more complicated aeroelastic trim problems for defined maneuvers. Occasional updates of the vehicle shape and the body-fitted computational grid yield an efficient convergence to aeroelastic equilibrium. An application to a generic rocket at supersonic flight demonstrates the process efficiency and exhibits significant aeroelastic effects on the aerodynamic stability derivatives.

Nomenclature

C_l = aerodynamic lift coefficient
C_l^n = lift coefficient at the nth trim update
$\bar{C}_l$ = requested lift coefficient
C_{l_α} = slope of C_l vs α
C_{l_0} = lift coefficient at $\alpha = 0$
C_m = aerodynamic moment coefficient
D = rocket diameter
E = energy per unit volume
$\{F_T\}$ = nonaxial thrust loads
H = total enthalpy
i, j, k = indices of the aerodynamic grid points; Figs. 2 and 3
J = number of grid points in the j direction
J_1 = $\min(J, j_{\text{in}} - 1)$
j_{in} = value of j for which adjacent i = const lines intersect
$[K]$ = generalized stiffness matrix
$[K_s]$ = discrete stiffness matrix
$[M]$ = generalized mass matrix
$[M_s]$ = discrete mass matrix
$\{N_z\}$ = aerodynamic force vector in structural grid
$\{\bar{N}_z\}$ = aerodynamic force vector in aerodynamic grid
p = pressure
T = thrust force
u, v, w = air velocity components
$\{V\}$ = vehicle velocity
X, Y, Z = components of the coordinate system; Fig. 4
$\{x_s\}$ = structural displacements
z = deflection to the Z direction
α = angle of attack
θ = rotation about the Y axis
$\{\xi\}$ = generalized displacement vector
ρ = air density
$[\phi]$ = set of low-frequency natural vibration modes
$[\phi_{z_l}]$ = row vector of modal deflections at X_l
$[\phi_{\theta_l}]$ = row vector of modal rotations at X_l
$[\omega_n]$ = natural frequencies taken into account

Subscripts

cg = center of gravity
cp = center of pressure
E = related to elastic modes
l = middle of the nozzle exit
n = number of trim update
R = related to rigid-body modes
0 = uniform rigid-body deflection of rotation

Received Aug. 29, 1996; presented as Paper 96-4012 at the AIAA/NASA/ISSMO 6th Symposium on Multidisciplinary Analysis and Optimization, Bellevue, WA, Sept. 4–6, 1996; revision received Aug. 1, 1997; accepted for publication May 6, 1998.

*Associate Professor, Faculty of Aerospace Engineering. Senior Member AIAA.
†Computational Fluid Dynamics Team Leader, Systems Group, Rocket Systems Division.
‡Dynamics Specialist, Systems Group, Rocket Systems Division. Member AIAA.

Introduction

STATIC aeroelasticity deals with steady fluid–structure interaction problems where coupling effects act in both directions, i.e., the airflow generates distortions of an elastic body in the airstream, and the distortions change the airstream parameters. This interaction must be considered in the design of flight vehicles because of its important effects on structural design loads and on aerodynamic stability coefficients. Integrated solutions that assume linear aerodynamics and elasticity are well established and incorporated in commercially available codes such as MSC/NASTRAN[1] and ASTROS.[2] However, there are vital questions about their boundaries of applicability. The linear approach might yield inadequate results in design-critical cases such as aircraft in transonic flight and missiles in supersonic flight. The source of inaccuracy in most cases is in the aerodynamics. More accurate solutions require the use of computational fluid dynamics (CFD) procedures.

Many Navier–Stokes and Euler-based CFD procedures were developed in recent years, some of them applicable to general three-dimensional configurations. Most procedures, such as those of Refs. 3–5, were applied with a fixed aerodynamic shape, namely with no flexibility or trim effects. The main practical difficulties in the application of these schemes are the work involved in the generation of a proper computational grid and the computer CPU time a full solution requires. Hence, the solution of aeroelastic problems for free-flight vehicles by iterative alternate full applications of a CFD code for a given shape and a finite element code for given loads, where each run defines the loads or shape for the following run, might be grossly impractical.

Some CFD codes were developed for dynamic aeroelastic analysis with unsteady flow. A survey of the status of these codes was presented in Ref. 6. The dynamic codes can be used to obtain static

solutions by letting the time-marching response achieve a steady state. Recent applications of this approach dealt with clamped models where inertial effects and trim conditions are ignored.[7–9] Locally varying time stepping and artificial structural damping were used in these applications to accelerate the static solution. Nevertheless, pseudodynamic static aeroelastic Navier–Stokes solutions for relatively simple wing–body configurations required huge computation time, typically several CPU hours per case on a Cray 2 computer.[8] Reference 9 demonstrated that the number of iterations required in these cases, with the aerogrid updated in each iteration, is similar to that required for a rigid case. It was also shown that the CPU time for structural computations including grid motion, with the structure represented by three low-frequency modes, was only about 10% of the total CPU time per iteration. This portion would probably be significantly larger in application to computationally lighter Euler cases with the structure represented by considerably more than three modes, as usually required for adequate static aeroelastic effects.[10,11]

The purpose of the work presented in this paper was to develop an efficient integrated computational scheme for static aeroelastic problems of maneuvering flexible flight vehicles with nonlinear aerodynamic effects. The main intended tasks of the presented scheme are the evaluations of structural design loads and aerodynamic stability derivatives with aeroelastic effects at flight conditions for which the aerodynamic nonlinearity is relatively mild. The scheme should be easily applicable with common CFD codes originally developed for steady flow around fixed shapes. Frequent updates of the vehicle shape and trim variables might be relatively expensive in these cases. Hence, the approach taken in this work was to base the solution on static equilibrium with a relatively small number of shape and trim updates. The solution is required to be applicable to free-free vehicles with inertia relief effects to allow a trim solution for a prescribed load factor and to account for follower thrust loads. The new scheme is applied in this paper to the analysis of a maneuvering rocket at supersonic powered flight.

Aerodynamic Model

The aerodynamic model was constructed for use by a general CFD code[3,4] that employs the three-dimensional unsteady Navier–Stokes equations. In our work we assume inviscid flow, which yields the simplified Euler equations. After the appropriate nondimensionalization, the equations are written in a Cartesian coordinate system (x, y, z) as

$$\frac{\partial}{\partial t}\bar{W} + \frac{\partial}{\partial x}\bar{F} + \frac{\partial}{\partial y}\bar{G} + \frac{\partial}{\partial z}\bar{H} = 0 \tag{1}$$

where

$$\bar{W} = [\rho \quad \rho u \quad \rho v \quad \rho w \quad \rho E]^T$$

$$\bar{F} = [\rho u \quad (\rho u^2 + p) \quad \rho uv \quad \rho uw \quad \rho uH]^T$$

$$\bar{G} = [\rho v \quad \rho uv \quad (\rho v^2 + p) \quad \rho vw \quad \rho vH]^T$$

$$\bar{H} = [\rho w \quad \rho wu \quad \rho wv \quad (\rho w^2 + p) \quad \rho wH]^T$$

The equations are to be solved numerically for $\bar{W}$.

The body-fitted computation grid is defined by a multiblock algorithm that allows local grid refinements. The far-field boundary conditions are defined according to the vehicle aerodynamic states such as angle of attack and pitch velocity. These define the flowfield at the far boundary of the finite domain of computations by using Riemann invariants for the direction normal to the boundary.[4] The boundary conditions at the surface of the vehicle are defined for nonviscid flow by zero-flux conditions.

The numerical scheme is a finite volume scheme using centered differencing plus artificial viscosity in space and an explicit Runge–Kutta scheme in time. A steady-state flow is assumed, which allows locally varying time stepping. Convergence is obtained when the residual, defined by the average value of $\Delta\rho/\Delta t$, is reduced by about five orders of magnitude.

The numerical application in this paper is for the generic rocket shown in Fig. 1 at supersonic Mach number. Side and rear views of the CFD grid of the rigid vehicle are shown in Figs. 2 and 3. The grid in each block is constructed by grid-point surfaces, indexed by $j = 1, J$, which surround the vehicle body, with the $j = 1$ surface fitting the body. The lines that connect the respective grid points of the surrounding surfaces form two other perpendicular surface sets, indexed by i and k as shown in Figs. 2 and 3. The origins of the $i =$ const surfaces form round cross sections along the rocket body. Each pair of neighboring cross sections forms an aerodynamic segment. The lift and moment at each aerodynamic segment are calculated by integrating its pressure distribution, multiplied by direction cosines with respect to the Z axis of Fig. 4. The resulting aerodynamic force vector is $\{\bar{N}_z\}$, where the ith term corresponds to the ith aerodynamic segment of the rocket.

The wraparound fins in our problem are tuned to provide adequate static stability and spin velocity, which generates some asymmetry in the pressure distribution due to angle of attack. The fins are assumed to be rigid in this work, and their total lift is added to the rocket body.

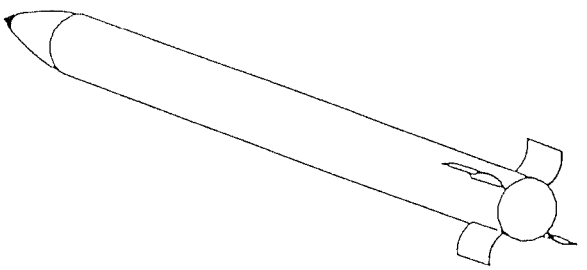

Fig. 1 Generic rocket with wraparound fins.

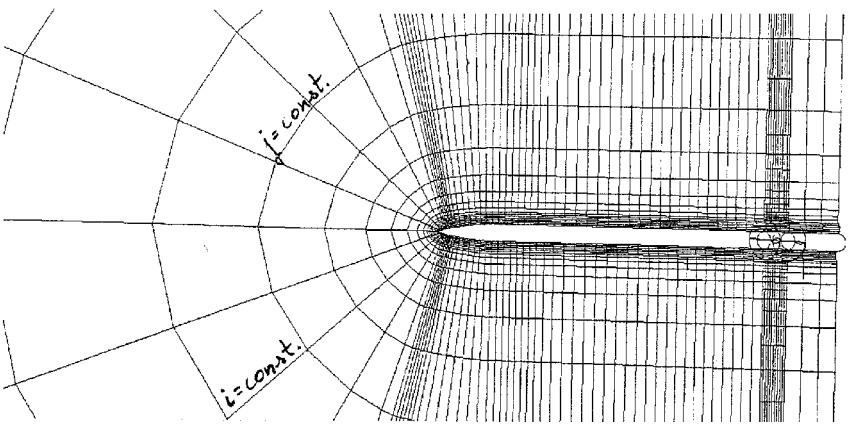

Fig. 2 Side view of the CFD grid.

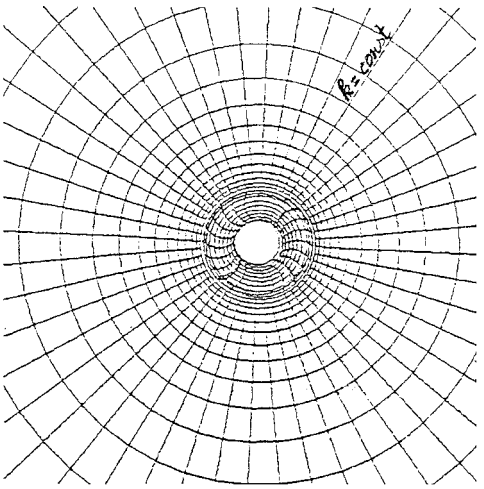

Fig. 3 Rear view of the CFD grid.

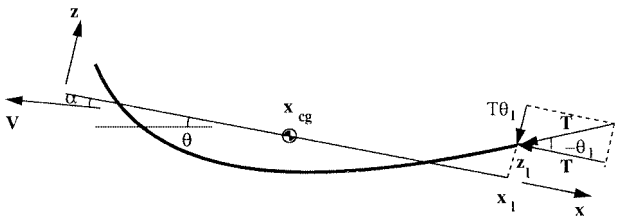

Fig. 4 Scheme of elastic deformations in the vertical plane.

Structural Model

A finite element model was used to construct the free-free structural mass and stiffness matrices $[M_s]$ and $[K_s]$. For the sake of clarity and simplicity we assume here that the rocket maneuvers in the vertical plane with negligible spin effects. A diagram of the elastic deformations in the vertical plane under aerodynamic, inertial, and thrust loads is shown in Fig. 4. It is assumed that the total drag and thrust forces of the undeformed rocket pass through its center of mass in the X direction. The coupling between aeroelastic, spin, and thrust misalignment effects in free-flight rockets is discussed in Ref. 12. The model is free to move as a rigid body in the Z (heave) and θ (pitch) directions. The equation of motion, ignoring structural damping, is

$$[M_s]\{\ddot{x}_s\} + [K_s]\{x_s\} = \{N_z\} + \{F_T\} \tag{2}$$

where the aerodynamic force vector $\{N_z\}$ is splined to the structural grid from aerodynamic loads in the aerodynamic grid[1] and the nonaxial thrust loads in $\{F_T\}$ are due to the deflection and rotation at the middle of the nozzle exit. The main effect of these thrust loads, in the context of static aeroelasticity, is on the rigid-body accelerations, as formulated later.

For computational efficiency and minimization of the structural data needed by the following integrated code, we use the modal approach that has been shown to be adequate in various linear static aeroelastic analyses.[10,11] The structural displacements are assumed in this approach to be a linear combination of a set of low-frequency natural vibration modes $[\phi]$ associated with $[M_s]$ and $[K_s]$, namely,

$$\{x_s\} = [\phi]\{\xi\} \tag{3}$$

Orthogonality implies diagonal generalized mass and stiffness matrices

$$[M] = [\phi]^T[M_s][\phi] \tag{4}$$

and

$$[K] = [\phi]^T[K_s][\phi] = [\omega_n]^2[M] \tag{5}$$

The first two modes in $[\phi]$ of our model are rigid-body modes. The first one is a uniform displacement z_0 to the Z direction, and the second is a rigid-body rotation θ_0 about an axis in the Y direction that passes through the center of gravity.

The substitution of Eq. (3) into Eq. (2) and premultiplication by $[\phi]^T$ yields the equation of motion in modal coordinates, which is partitioned according to rigid-body and elastic modes as

$$\begin{bmatrix} M_{RR} & 0 \\ 0 & M_{EE} \end{bmatrix}\begin{Bmatrix} \ddot{\xi}_R \\ \ddot{\xi}_E \end{Bmatrix} + \begin{bmatrix} 0 & 0 \\ 0 & K_{EE} \end{bmatrix}\begin{Bmatrix} \xi_R \\ \xi_E \end{Bmatrix} = \begin{bmatrix} \phi_R^T \\ \phi_E^T \end{bmatrix}\{N_z\} + T\begin{bmatrix} T_{RE} \\ 0 \end{bmatrix}\{\xi_E\} \tag{6}$$

where

$$[T_{RE}] = \begin{bmatrix} 0 & z_0 \\ -\theta_0 & \theta_0(X_{cg} - X_l) \end{bmatrix}\begin{bmatrix} \phi_{z_l} \\ \phi_{\theta_l} \end{bmatrix}$$

The effects of the thrust deflection on the elastic modes are assumed to be negligible.

The effects of elastic accelerations $\{\ddot{\xi}_E\}$ are neglected in the static aeroelastic investigation. Consequently, the elastic modal deformations $\{\xi_E\}$ under given aerodynamic loads are easily calculated from the second row of Eq. (6). The use of normal modes as generalized coordinated implies that inertia-relief effects are included automatically.[11] This is an important advantage over the discrete-coordinate static aeroelastic analysis for free-free vehicles,[1,2] which requires explicit calculation of the inertial loads, and the application and removal of supports to bypass the singularity of $[K_s]$. Once $\{\xi_E\}$ is calculated, the rigid-body accelerations can be calculated by the top row of Eq. (6), and the actual elastic deformations can be recovered by Eq. (3).

The number of lowest-frequency modes that should be taken into account strongly depends on the application. Previous applications with linear aerodynamics showed good results with 20 modes for high-aspect-ratio wing cases[11] and 30 modes for fighter-aircraft cases.[10] In our application, where the rocket structure is fairly simple and the fins are assumed to be rigid, the two rigid-body modes and the first four bending modes in the vertical plane yield very accurate static aeroelastic results.

Integrated Aeroelastic Analysis

The integrated solution is performed by introducing shape corrections during the CFD convergence process. The only data needed for calculating the modal deformations by Eqs. (3) and (6) are the diagonal $[K_{EE}]$ and the shapes $[\phi_E]$ associated with the considered modes. The effect of the elastic deformations on the CFD computation grid should be tailored to the specific application. A simple algorithm for deflecting the grid around aircraft wings is given in Ref. 6. In our case, to obtain the distorted rocket shape and the CFD grid around it, we assume that the transverse cross sections of the rocket remain undeformed and normal to the neutral axis. We define the new grid by translation and rotation of each line in an $i = \text{const}$ surface, for $1 \le j \le J_1$, according to the elastic deformations obtained for the ith cross section by interpolation from the structural grid.

The integrated computation procedure is first described for the case of fixed vehicle aerodynamic states such as angle of attack and control-surface deflection angle. As described earlier, the convergence criterion for a regular CFD run with fixed geometry is the reduction of five orders of magnitudes of the residual. This typically requires between several hundred and several thousand CFD iterations, depending on the application complexity. The computation should start with a number of iterations that reduce the residual by about two orders of magnitude for the rigid shape (or a better initial estimate of the deformed shape if available). After that, it is recommended that the deformations and the computation grid be updated after each residual reduction of about one order of magnitude. The added CPU time and storage are very small compared with those of a regular CFD run.

The vehicle aerodynamic states are divided into two categories: global aerodynamic states, such as angle of attack and pitch rate, and control-surface deflection angles. The aerodynamic states define the flow conditions far from the vehicle, and the control variables are

defined by deflecting the CFD grid blocks in a way similar to the distortions due to elastic deformations. In many static aeroelastic analysis cases, such as in maneuver loads analysis, the user defines some or all of the rigid-body accelerations, leaving the related aerodynamic and control variables to be defined by the analysis such that the first row in Eq. (6) is satisfied. This trimming process requires an estimate of the aerodynamic derivatives, such as the lift-curve slope C_{L_α}. The derivative estimates are not required to be very accurate for convergence to trim conditions. The computation process starts at an initial guess and proceeds with additional trimming updates between the elastic updates, as demonstrated in the following numerical example.

The nominally axial thrust of Fig. 4 affects the trim equations without affecting the elastic deformations directly, as indicated in Eq. (6). When thrust vectoring is used for maneuvering the vehicle, the vertical thrust component is treated like control-surface loads that affect both rows of Eq. (6).

The proposed approach can also accommodate structural nonlinearity by modifying the generalized stiffness and mass matrices in Eq. (6) without changing the modal coordinates. The property updates cause these matrices to become nondiagonal. As described in Ref. 13, even large structural changes can be accommodated by this approach, providing they are confined to a small number of known locations. Large fictitious masses were used in Ref. 13 to load the locations of variable structural properties when the modes are calculated. The effects of these masses on the vehicle mass properties were removed after the modes were calculated, and the process proceeded in the regular way with the stiffness changes accounted for accurately.

Numerical Applications

All of the numerical results that follow are for the case of the generic rocket of Fig. 1 at Mach 3.5 and angle of attack $\alpha = 5$ deg. The rocket length is 3.3 m, its body diameter is $D = 0.16$ m, its weight is 108 kg, and its c.g. is at $x_{cg} = 1.175$ m. The first case is with no trim, namely, α defined by the user, and with no thrust. The structural deformations are represented by four elastic modes. The residual convergence histories of four different cases, a rigid one (for reference) and three deformed ones, are shown in Fig. 5. The only differences between the deformed cases are the first deformation points that were at 25, 50, and 75 iterations, respectively. After the first one, deformation updates in all of the cases were performed after each residual reduction factor of 10. Each update caused a residual spike that is smaller and recovered faster as convergence is approached. The total number of iterations for residual reduction of five orders of magnitude is 141 for the rigid case and 147, 155, and 169 for the deformed case. In other words, the cost for solving the aeroelastic case was only between 4 and 20% larger than that of the rigid case. Based on this example and other trial runs, we recommend performing the first deformation after a residual reduction factor of about 100. An earlier deformation might cause a numerical divergence (not shown).

The lift distributions along the rocket for the rigid and deformed converged solutions are given in Fig. 6. Because most of the loads are concentrated at the front and rear ends, whereas the weight is more evenly distributed, the rocket deforms in a banana shape, similar in nature to that of Fig. 4. Consequently, the nose increases its local angle of attack, which increases the nose loads, whereas the opposite happens at the rear part. The deformations are quite small, a maximum of about 0.5 mm at the nose, but their effect on the total lift and moment coefficients C_l and C_m might be significant. The variations of C_l and C_m along the structural updates of the deform1 case in Fig. 5 are given in Figs. 7 and 8. The elastic deformations move the c.p. $x_{cp} = -D \times C_m/C_l$ forward, from $4.390D$ to $4.027D$ behind the c.g. This reduction of $0.373D$ in the static stability margin is not very significant for this highly stable rocket but might be very significant for missiles that have low stability margins for high maneuverability.

The aerodynamic loads of the deformed case in Fig. 6, plus the inertial loads due to the associated heave and pitch accelerations, were applied to the full finite element model in a static analysis. The resulting elastic deformations were practically identical to those obtained by the new integrated CFD scheme, which shows that the use of four modes was adequate.

A thrust force of 120,000 N was added to evaluate its effect on the aerodynamic coefficients. The structural deformations cause a nose-up thrust moment that moves x_{cp} forward by an additional $0.02D$. This is a small effect in our case but can be more significant with rockets or missiles with larger length, flexibility, or thrust.

To check the integrated approach for a trim case, the converged $\bar{C}_l = 0.742$ of the previous case was defined as a user-input parameter, leaving the iterative code to converge to this parameter by trimming α at selected update points along the computation path, starting with an initial guess α_1. The angle of attack is determined at the nth update point by

$$\alpha_{n+1} = \frac{\bar{C}_l - C_{l_0}}{C_l^n - C_{l_0}} \alpha_n \tag{7}$$

where $C_{l_0} = 0$ in our case. With zero thrust, the process should converge in our example to $\alpha = 5$ deg (the input to the previous case).

A sample convergence process, with an initial $\alpha_1 = 3$ deg, is shown in Fig. 9, where the trim points and deformation points are marked differently. As in the previous case, the process started with 25 iterations for a rigid rocket, followed by a deformation update.

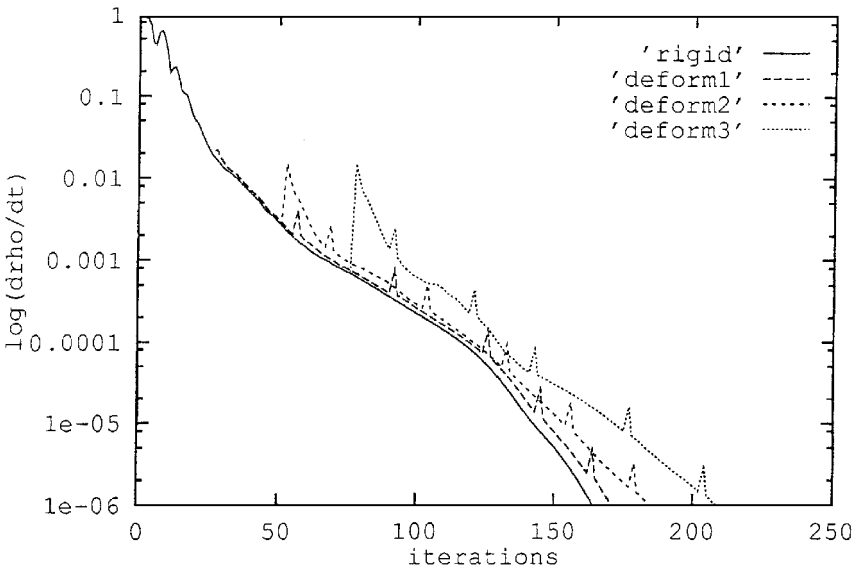

Fig. 5 Convergence history for rigid and deformed cases; $M = 3.5$ and $\alpha = 5$ deg.

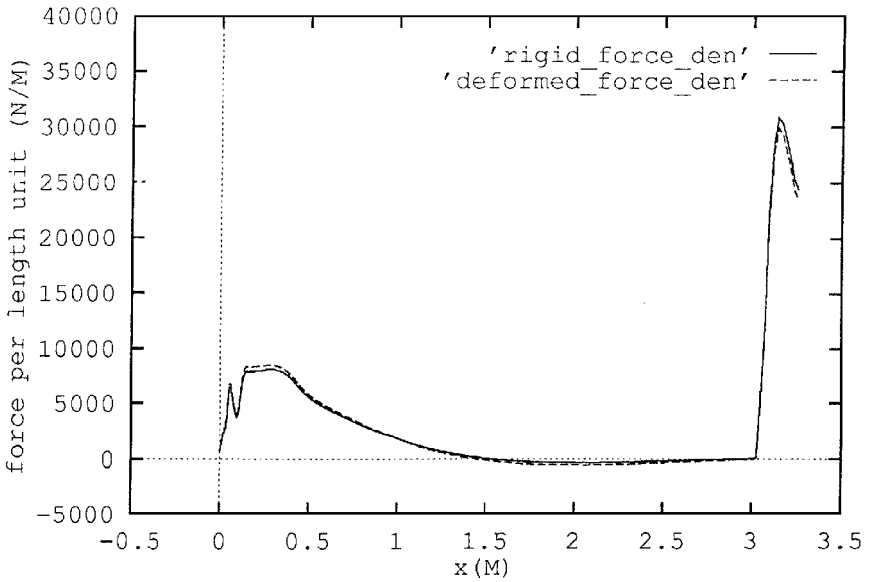

Fig. 6 Lift distribution for rigid and deformed cases; $M = 3.5$ and $\alpha = 5$ deg.

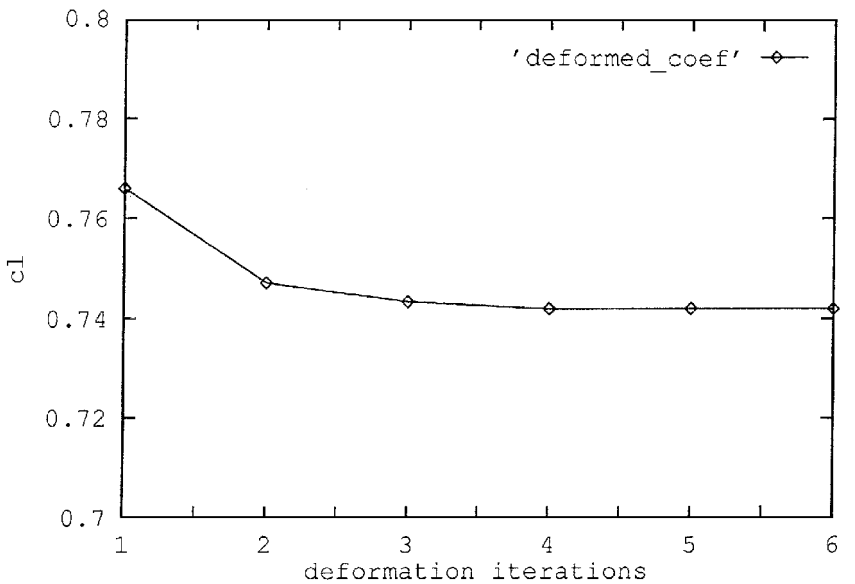

Fig. 7 Total lift coefficient along the computation path; $\alpha = 5$ deg.

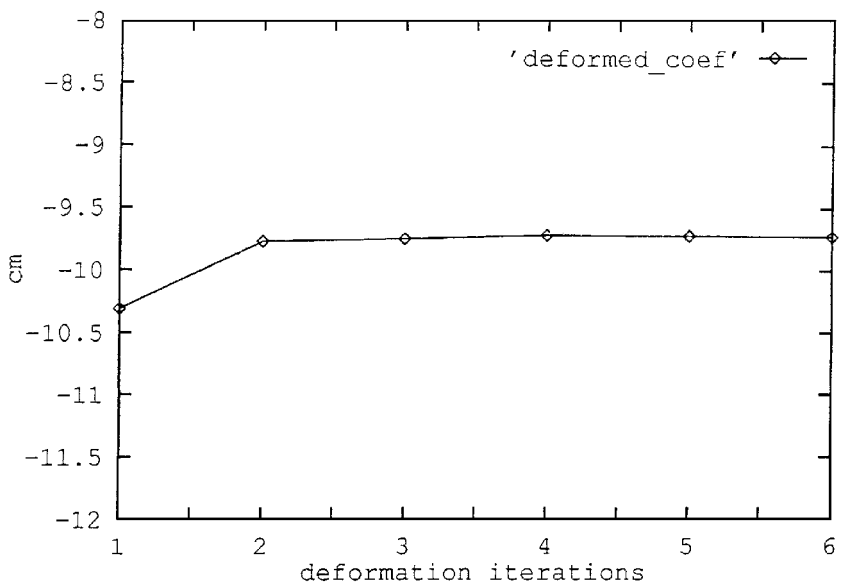

Fig. 8 Total moment coefficient along the computation path; $\alpha = 5$ deg.

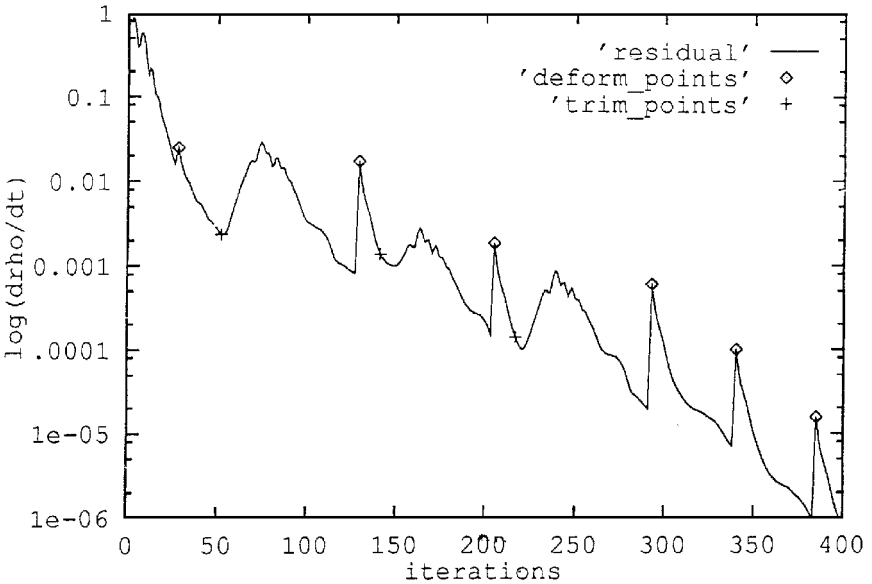

Fig. 9 Convergence history for aeroelastic solution with trim; $M = 3.5$ and $\bar{C}_l = 0.742$.

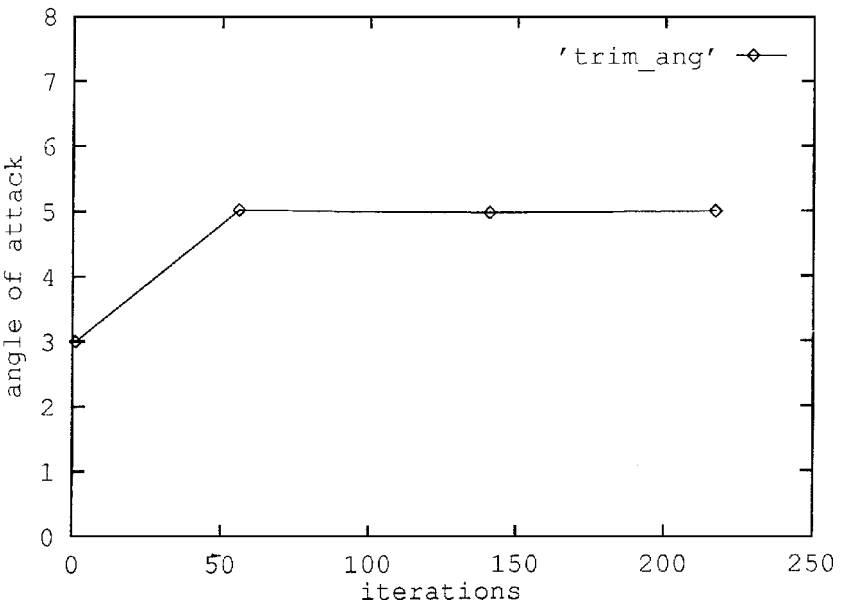

Fig. 10 Angle of attack in degrees at trim updates along the CFD iterations.

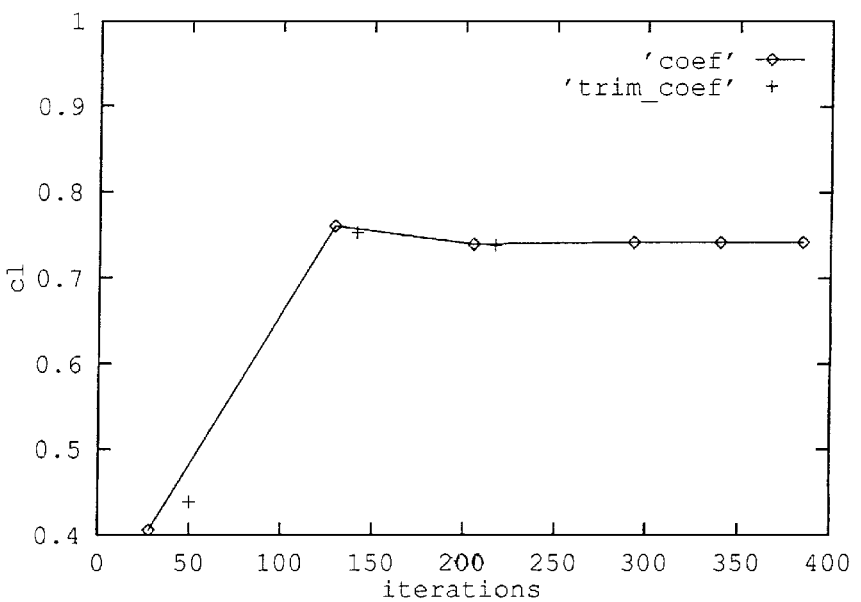

Fig. 11 Total lift coefficient along the computation path; trim case with $\bar{C}_l = 0.742$.

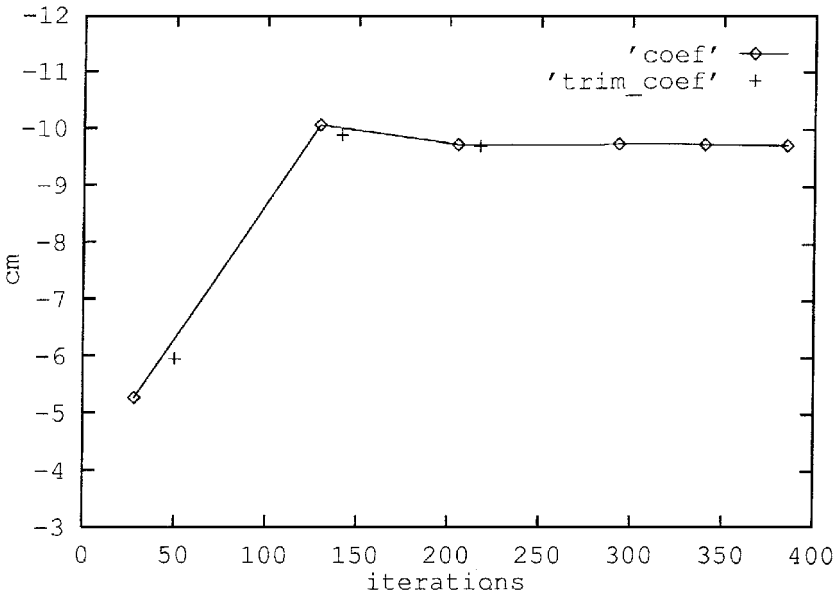

Fig. 12 Total moment coefficient along the computation path; trim case with $\bar{C}_l = 0.742$.

From this point there were alternate deformation and α updates every time the residual was reduced by a factor of 10 or when the number of iterations since the previous deformation update exceeded 100. Also, when the α increment was less than 0.001 deg, the trim update was not performed. We can see that the residual response to a trim update is very different from the spiky response to a deformation update. This is because the immediate effect of a trim update is on the far-field conditions. A number of CFD iterations pass before the effects of the far-field changes reach the vehicle surface. In general, the addition of trim iterations reduces the residual convergence rate. The total number of iterations for residual reduction of five orders of magnitude in the aeroelastic trim case of Fig. 9 is about twice that of the aeroelastic case with a fixed angle of attack in Fig. 5.

The values of angle of attack after the trim updates vs the number of CFD iterations are shown in Fig. 10. The lift and moment coefficients C_l and C_m just before the deformation updates are shown in Figs. 11 and 12, respectively. The coefficient values just before the trim updates are also shown. It is clear that the global aerodynamic coefficients and the associated trim variables converge rapidly, which means that the strategy of performing trim changes at a few CFD points only is adequate. Specifically, the lift coefficient reaches the desired value of $\bar{C}_l = 0.742$ after about 150 iterations.

Conclusions

An efficient integrated solution for computational static aeroelastic problems has been presented. The process is based on a regular body-fitted CFD solver, with several shape and boundary condition changes due to structural deformations and trim changes during the residual convergence process. With the use of modal coordinates, the computational cost of the structural deformations is negligible compared with the CFD cost. An application of the new scheme to a free-flight powered rocket showed significant aeroelastic effects on the vehicle aerodynamic coefficients and stability margins. The ratio between the number of iterations required for aeroelastic solutions and those required for the rigid rocket was up to 1.2 for aeroelastic cases with no trim and 2.0 for aeroelastic trim cases. It is recommended that one start the CFD process with a residual reduction factor of about 100 before starting the structural deformations and an additional reduction factor of 10 before starting the trim updates.

References

[1]Rodden, W. P., and Johnson, H. J., "MSC/NASTRAN Aeroelastic Analysis User's Guide," MacNeal–Schwendler Corp., Los Angeles, CA, Oct. 1994, pp. 35-49.

[2]Neill, D. J., Johnson, E. H., and Canfield, R. A., "ASTROS—A Multidisciplinary Automated Structural Design Tool," *Journal of Aircraft*, Vol. 27, No. 12, 1990, pp. 1021–1027.

[3]Jameson, A., Schmidt, W., and Turkel, E., "Numerical Solution of the Euler Equations by Finite Volume Methods Using Runge–Kutta Time Stepping Schemes," AIAA Paper 81-1259, June 1981.

[4]Jameson, A., and Baker, T. J., "Solution of the Euler Equations for Complex Configurations," AIAA Paper 83-1929, July 1983.

[5]Vasta, V. N., and Wedan, B. W., "Development of a Multigrid Code for 3-D Navier–Stokes Equations and Its Application to Grid Refinement Study," *Computers and Fluids*, Vol. 18, No. 4, 1990, pp. 391–403.

[6]Edwards, J., and Malone, J. B., "Current Status of Computational Methods for Unsteady Transonic Unsteady Aerodynamics and Aeroelastic Analysis," AGARD Structural and Materials Panel Specialist's Meeting on Transonic Unsteady Aerodynamics and Aeroelasticity, Paper 1, Oct. 1991.

[7]Schuster, D., Vadyak, J., and Atta, E., "Static Aeroelastic Analysis of Fighter Aircraft Using a Three-Dimensional Navier–Stokes Algorithm," AIAA Paper 90-0435, Jan. 1990.

[8]Lee-Rauch, E. M., and Batina, J. T., "Wing Flutter Boundary Prediction Using Unsteady Euler Aerodynamic Method," *Journal of Aircraft*, Vol. 32, No. 2, 1995, pp. 416-422.

[9]Obayashi, S., and Guruswamy, G. P., "Convergence Acceleration of Navier–Stokes Solver for Efficient Static Aeroelastic Computations," *AIAA Journal*, Vol. 33, No. 6, 1995, pp. 1134–1141.

[10]Sheena, Z., and Karpel, M., "Static Aeroelastic Analysis Using Aircraft Vibration Modes," *Proceedings of the 2nd International Symposium of Aeroelasticity and Structural Dynamics*, DGLR, Bonn, Germany, 1985, pp. 229–232.

[11]Karpel, M., and Brainin, L., "Stress Considerations in Reduced-Size Aeroelastic Optimization," *AIAA Journal*, Vol. 33, No. 4, 1995, pp. 716–722.

[12]Livshits, D. S., Yaniv, S., and Karpel, M., "Dynamic Stability of Free Flight Rockets," *Proceedings of the AIAA/ASME/ASCE/AHS/ASC 37th Structures, Structural Dynamics, and Materials Conference*, AIAA, Reston, VA, 1996, pp. 230–236 (AIAA Paper 96-1344).

[13]Karpel, M., and Wieseman, C. D., "Modal Coordinates for Aeroelastic Analysis with Large Local Structural Variations," *Journal of Aircraft*, Vol. 31, No. 2, 1994, pp. 396-403.

R. M. Cummings
Associate Editor